



Rapid simulations of hyperspectral near-field images of three-dimensional heterogeneous surfaces

XINZHONG CHEN,^{1,7}  ZIHENG YAO,¹  STEFAN G. STANCIU,²  D. N. BASOV,³ RAINER HILLENBRAND,^{4,5} AND MENGKUN LIU^{1,6,8}

¹Department of Physics and Astronomy, Stony Brook University, Stony Brook, New York 11794, USA

²Center for Microscopy-Microanalysis and Information Processing, Politehnica University of Bucharest, Bucharest 060042, Romania

³Department of Physics, Columbia University, New York, New York 10027, USA

⁴CIC nanoGUNE BRTA and Department of Electricity and Electronics, UPV/EHU, Donostia-San Sebastián 20018, Spain

⁵IKERBASQUE, Basque Foundation for Science, Bilbao, Spain

⁶National Synchrotron Light Source II, Brookhaven National Laboratory, Upton, New York 11973, USA

⁷xinzhong.chen@stonybrook.edu

⁸mengkun.liu@stonybrook.edu

Abstract: The scattering-type scanning near-field optical microscope (s-SNOM) has emerged as a powerful tool for resolving nanoscale inhomogeneities in laterally heterogeneous samples. However, most analytical models used to predict the scattering near-field signals are assuming homogenous landscapes (bulk materials), resulting in inconsistencies when applied to samples with more complex configurations. In this work, we combine the point-dipole model (PDM) to the finite-element method (FEM) to account for the lateral and vertical heterogeneities while keeping the computation time manageable. Full images, spectra, or hyperspectral line profiles can be simulated by calculating the self-consistent dipole radiation demodulated at higher harmonics of the tip oscillation, mimicking real experimental procedures. Using this formalism, we clarify several important yet puzzling experimental observations in near-field images on samples with rich typography and complex material compositions, heterostructures of two-dimensional material flakes, and plasmonic antennas. The developed method serves as a basis for future investigations of nano-systems with nontrivial topography.

© 2021 Optical Society of America under the terms of the [OSA Open Access Publishing Agreement](#)

1. Introduction

The scattering-type scanning near-field optical microscope (s-SNOM) utilizes a sharp and usually metalized atomic force microscope (AFM) tip to enhance the local focusing of light, achieving deep subwavelength spatial resolution [1,2]. The near-field electrostatics between the tip and sample surface is complex, which poses obstacles in performing quantitative analysis on the nano-imaging and nano-spectroscopy data. Despite recent advances [3–9], many puzzling experimental observations regarding s-SNOM measurements remain unresolved or only empirically examined. For example, what causes the anomalous near-field signal when scanning across a steep sample edge? How does the roughness of the sample surface influence the local field and the scattering signal? What causes the asymmetric near-field contrast over a plasmonic antenna? This work sheds light on the above questions by combining the numerical finite-element method (FEM) with the point-dipole model (PDM) formalism, which enables complex simulations that are previously difficult or even impossible.

Among different physical models [10–13], the rudimentary PDM is nonetheless effective in many s-SNOM modeling tasks. It approximates the tip as a point-dipole located at the tip apex [1,14]. Despite the seemingly idealized approximation, the PDM is widely used because of

its simplicity and the fact that it offers a clear and intuitive physical picture. It captures many key aspects of the near-field tip-sample interactions including the momentum distribution [15]. Consequently, its popularity remains high despite the availability of more sophisticated models [15–19].

The analytical solution of the PDM is restricted to homogeneous bulk samples and layered samples with in-plane translational symmetry [15,20]. Lateral heterogeneity in the nanoscale can not be easily accounted for since the momentum-dependent reflection coefficient is ill-defined. This shortcoming of the PDM is also commonly shared by other (more rigorous) models [10–13]. Numerical full-wave simulations with realistic tip geometry, on the other hand, have been demonstrated to be a possible route to resolve the lateral heterogeneity. However, the significant scale mismatch between the wavelength and the tip-sample distance demands prohibitive computation power, making simulations with variable tip positions (imaging) and light frequencies (spectroscopy) formidable tasks [21–24]. A recent study investigates the field distribution around a sphere near the sample surface, demonstrating again that even a simple model captures the tip-sample interaction well and can act as a valid approximation [25]. However, the radiation of the sphere is yet to be considered carefully. Therefore, a computationally efficient extension of the PDM for arbitrarily heterogeneous sample surfaces is imperative.

In this article, we combine the FEM with the PDM framework to demonstrate unprecedented fast simulations of both nano-imaging and nano-spectroscopy experiments, including signal modulation by tip oscillation and signal demodulation at higher harmonics on arbitrary sample surfaces. As a proof-of-concept demonstration, we investigate a wide range of examples including topography-induced near-field contrast, surface plasmon polariton in graphene nanostructures, and the plasmonic response of optical antennas. Our proposed method has the advantages of being highly versatile, computationally efficient, and easy to implement and interpret. When the algorithm is parallelized into multiple CPU cores, a high-resolution near-field imaging simulation can be performed in a matter of hours while the simulation of a typical near-field spectrum lies in the range of tens of minutes with a commercial-grade desktop. When certain symmetry conditions such as rotational symmetry can be exploited, the computational time can be further compressed significantly. Compared to simulations with realistic tip modelling, our method is at least one order of magnitude faster due to its electrostatic nature and intrinsically smaller simulation volume.

2. Working principle of s-SNOM and the PDM framework

First, we briefly summarize the working principle of s-SNOM [26] and the general PDM framework. In s-SNOM coherent laser radiation is focused onto an AFM tip by diffraction-limited optics such as an off-axis parabolic mirror. The light polarizes the tip, whose induced dipole moment is further modified via the near-field tip-sample interaction [24]. This modification of the dipole moment contains local information about the sample underneath the tip apex and can be detected as the field scattered into the far-field. To suppress the overwhelming background scattering not related to the near-field interaction of interest, the AFM is operated in tapping mode. The vertical oscillation of the tip modulates the near-field interaction at the tapping frequency Ω , which usually lies in the range of tens to hundreds of kHz. Consequently, a lock-in amplifier is used to demodulate the optical signal at higher harmonics ($n = 2, 3, \dots$) of Ω , which represents the manifestation of the genuine near-field information.

The PDM was introduced along with the first-generation s-SNOM instruments to describe the imaging contrast mechanism [2,14,27]. In the PDM, the AFM tip is approximated as a point-dipole located at the center of a sphere. That is, we consider a quasi-electrostatic problem of a polarizable point-dipole located above the sample surface under exposure to an external electric field. For the rest of the article, the terms “tip” and “point-dipole” will be used interchangeably. We typically only consider the dipole moment in the vertical direction due to the elongated AFM

tip geometry and p-polarized incident light that is typically used. In the rest of the article, we discuss only the vertical dipole moment unless otherwise noted. Full vector dipole moment can be considered in a similar fashion by considering the full polarizability tensor as discussed in section 3.3. The (vertical) dipole moment p can be written as a superposition of the external field E_{ext} and the induced field E_{ind} in the vertical direction:

$$p = \alpha(E_{ext} + E_{ind}), \quad (1)$$

where $\alpha = 4\pi a^3 \frac{\epsilon_t - 1}{\epsilon_t + 2}$ is the bare polarizability, a is the effective radius, and ϵ_t is the dielectric function of the tip material. Since in the vast majority of cases of real applications a metallic tip is used, we take $\alpha = 4\pi a^3$ in the simulations. Notice that E_{ind} is proportional to p , and thus can be written as $E_{ind} = pG$, where G can be interpreted as the field due to a unit dipole at the dipole position. This field is the direct result of the charge accumulation on the sample induced by the unit dipole. Since p appear on both sides of Eq. (1), it describes the iterative interaction between the substrate and the dipole self-consistently. Combined with Eq. (1) we have

$$p = \alpha_{eff} E_{ext} = \frac{\alpha}{1 - \alpha G} E_{ext}. \quad (2)$$

The detected scattering is proportional to α_{eff} and the n -th harmonic demodulated signal is given by

$$S_n = \int_0^T \alpha_{eff} e^{-in\Omega t} dt, \quad (3)$$

which can be directly compared to the experimentally collected data. Here the tip motion is assumed to be harmonic oscillation. For homogenous bulk sample, the method of image charge applies and E_{ind} can be simply regarded as the field due to the image dipole of dipole moment $p' = \beta p$, where $\beta = \frac{\epsilon - 1}{\epsilon + 1}$ and ϵ is the sample dielectric function. Therefore, we return to the familiar expression

$$G = \frac{\beta}{16\pi(z+a)^3} \text{ and } \alpha_{eff} = \frac{\alpha}{1 - \frac{\alpha\beta}{16\pi(z+a)^3}} \quad (4)$$

where $z + a$ is the distance between the point-dipole and the sample surface [14]. More generally, $G = \int_0^\infty q^2 e^{-2q(z+a)} r_p(q, \omega) dq$, where q is the in-plane momentum and $r_p(q, \omega)$ is the momentum- and frequency-dependent reflection coefficient for p-polarized light. One can immediately see that the key to adapting the PDM to arbitrary surfaces is the evaluation of G . Problems arise when the method of image charge fails to apply in cases where the sample surface exhibits heterogeneity. Analytical expression of G is not easy to obtain in general.

To account for the secondary far-field reflections off the sample surface, a multiplicative far-field factor defined as $(1 + r)^2$ is often included in the formulation, where r is the far-field Fresnel reflection coefficient. $(1 + r)E_{ext}$ is essentially the illumination field at the tip position. In our formalism, we do not explicitly discuss this effect for simplicity. In principle it can be integrated by simulating the field at the dipole position due to an incident plane wave.

3. Integration of the FEM and the PDM

3.1. Validity and accuracy test

Next we demonstrate that the numerical evaluation of G for arbitrarily heterogeneous sample surfaces can be done straightforwardly in a time-efficient manner with a commercial-grade desktop computer (CPU: Intel i9 10850 K, RAM: 64 GB). Numerical solvers with optimized algorithms for Maxwell's equations are widely available. Popular techniques include the FEM [28], the finite-difference time-domain method (FDTD) [29], and the method of moment (MOM) [30]. These techniques can all be used to solve the problem at hand in principle. In this work, we demonstrate our approach using a FEM solver (COMSOL Multiphysics) as FEM is highly

versatile and suitable for simulating a variety of materials such as geometrically thin and optically anisotropic structures.

In the 3D quasi-electrostatic simulations, the point-dipole has a polarizability $4\pi a^3$. For simplicity, we create an electric point-dipole of unit dipole moment. The sample with arbitrary geometry and various properties is modeled below the point-dipole (see an example of the simulation setup in [Supplement 1](#)). A few examples include thin films, samples with topographic features, 2D materials supporting surface polaritons, and plasmonic antennas as schematically shown in Fig. 1(a). The whole simulation domain, typically a sphere or cylinder, has a size that is much larger than a in all three dimensions. The boundary condition is set such that the potential at the simulation domain boundaries is zero. For quasi-electrostatics the governing equation is simply $-\nabla \cdot \nabla V = \rho_f$, where V is the potential and ρ_f is the free charge density. The mesh size is ensured to be much smaller than a around the dipole and sample surface to capture the field and charge distribution accurately. Once the simulation is done, physical quantities such as the electric field \mathbf{E} and polarization density \mathbf{P} are known everywhere within the simulation domain. The evaluation of G can be done in two ways – a physical one and a numerical one. The former one requires the computation of the induced charge distribution on the sample surfaces and volumes. That is, the induced surface charge density is given by $\sigma = \hat{\mathbf{n}} \cdot (\mathbf{P}_2 - \mathbf{P}_1)$ and the induced volume charge density is given by $\rho = \nabla \cdot \mathbf{P}$, where $\hat{\mathbf{n}}$ is the unit surface normal, \mathbf{P} is the polarization density, and $\mathbf{P}_{1,2}$ refers to the polarization density on both sides of a surface. G can be calculated by integrating the charge density over all the surfaces and volumes using Coulomb's law. It is important to realize that this approach is different from the previous simulation methods with realistic tip modelling [24,31], where the dipole moment of the tip is calculated by integrating the charge density on the tip surface. In the numerical way, two simulations need to be executed. One simulation with the sample of its actual dielectric function and another simulation with a sample composed of vacuum ($\epsilon = 1$). G can be obtained by evaluating the difference in the electric fields directly at the dipole position in both simulations. Once G is computed, either physically or numerically, S_n can be calculated by Eqs. (2) and (3). Evaluating G using the physical approach only requires a single simulation thus is preferable in terms of time efficiency.

First we test the accuracy of the simulation to determine the appropriate mesh density. This can be done by simulating a homogeneous sample and comparing the result to the analytical expression in Eq. (4). We use SiO_2 as an example as its mid-IR resonant response is distinct and well characterized. The dielectric function of SiO_2 in the mid-infrared regime can be found in literature [32]. The numerically simulated S_2 amplitude and phase are shown in Fig. 1(b) along with analytical calculations using Eq. (4). The consistency is excellent, confirming the validity and accuracy of the simulation method. This simulation only takes a few minutes as the system possesses rotational symmetry. In both the simulation and the calculation, we assume $a = 30$ nm, and the tip oscillation amplitude $A=50$ nm. The minimum tip-sample distance is $h_0 = 1$ nm. These are generic experimental parameters and can be tuned accordingly. Without loss of generality, they will be used throughout the subsequent simulations. The spectra are normalized to the spectrum on intrinsic Si, which has a constant dielectric function $\epsilon_{\text{Si}} = 12$ throughout the relevant spectral range. This convention applies to the simulations in the rest of the article unless otherwise noted. S_n with $n>2$ can be simultaneously obtained but since all the S_n show a similar trend, we mainly display S_2 in the subsequent sections. Note that to perform the Fourier integral numerically in Eq. (3) we need to compute α_{eff} at various tip-sample distances. We find that sampling the tip-sample distance in a logarithmic scale at only 6 points then linearly interpolating them is sufficient to yield the accurate numerical integral in most cases (see [Supplement 1](#)) since the near-field interaction is the strongest when the distance is small and decays rapidly as the distance increases. To ensure accuracy all the simulations are done with at least 8 vertical tip-sample distances.

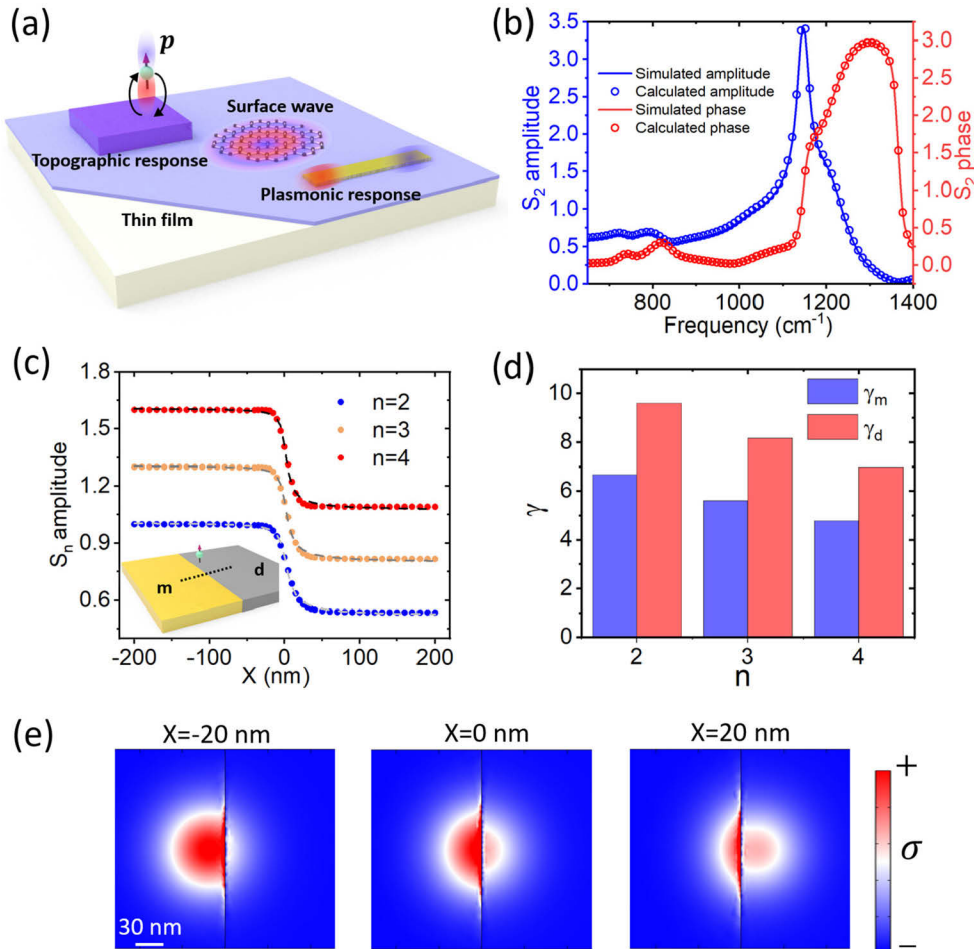


Fig. 1. Schematics of the simulated samples and simulation accuracy check. (a) Schematic representation of various heterogeneous samples that can be simulated using our versatile method. (b) Numerically simulated near-field amplitude and phase spectra of bulk SiO_2 compared to the analytical expression in Eq. (4). The achieved excellent consistency confirms the accuracy of our simulation. A suitable spatial mesh density can be identified by accessing the convergence of the simulation result to the analytical expression. (c) Simulated near-field amplitude line profiles (dots) across a flat metal-dielectrics boundary. The profiles are fitted by the equation proposed in [23]. The profiles are vertically shifted for clarity. The inset shows the schematics of the metal-dielectrics boundary. The dotted line indicates the scan path. (d) The fitting parameters γ_d and γ_m for different harmonics of the tip oscillation frequency. (e) Visualization of the surface charge distribution as the tip scans across the boundary (from left to right). For these specific plots, the tip-sample distance is kept at 80 nm.

Next we characterize the spatial response of our simulation using a heterogeneous sample surface with a flat metal-dielectrics boundary [inset in Fig. 1(c)]. Here we consider $\varepsilon_m = -10^4 + 10^4i$ and $\varepsilon_d = 4$. The boundary coincides with $X = 0$ and the tip is scanned across the boundary at fine steps while oscillating in the vertical direction. Figure 1(c) displays the near-field amplitude profiles (dots) demodulated at different harmonics of the tip oscillation. The profiles are fitted (dashed lines) by the equation proposed in Ref. [23], where γ_m and γ_d are the fitting parameters that describe the widths of the profiles on the metal and dielectric sides respectively. The best fit values of γ_m and γ_d are shown in Fig. 1(d). It can be clearly seen that γ_m is smaller than γ_d . Furthermore, γ decreases with increasing demodulation order n . This is due to the well-known fact that the tip's near field is more confined when it probes a metal sample as compared to a dielectric sample. Further, the near-field signal yields information about a spatially more confined area when the demodulation order is increased. Our observations are consistent with the previous study using more sophisticated tip modeling [23], which validates the physical rigor of our simple PDM formalism. As discussed in the previous section, the key driver of the near-field contrast in the PDM is the induced surface charge, which is plotted in Fig. 1(e) for different tip positions.

3.2. Simulation of topographically heterogeneous samples

Next we demonstrate an important application of our method – the simulation of heterogeneous sample surfaces with topographic features. We stress that it is fundamentally important to study topography-induced near-field contrasts because they have been experimentally observed on a routine basis (see literature examples in Supplement 1). In experiments, the topography-induced near-field contrast is often convoluted with the genuine optical contrast. Incorrect interpretation could potentially result in misleading and invalid conclusions of the sample properties. In this article we mainly discuss three types of common topography-induced near-field contrasts: the edge darkening effect, surface curvature effect, and finite size effect.

3.2.1. Edge darkening effect

The first example used here is a 500 nm by 500 nm by 30 nm PMMA square on Si substrate as schematically depicted in Fig. 2(a). The dielectric function of PMMA can be found in [33]. The tip is raster-scanned over the square following its topography (Fig. 2(b)) to generate a near-field image according to the dielectric function of PMMA at the desired frequency. This type of monochromatic imaging simulation with a fine spatial resolution typically takes about ten hours. Figure 2(c) and (d) show S_2 amplitude and phase images at $\omega = 1500 \text{ cm}^{-1}$, where PMMA exhibits no absorption. Figure 2(e) and (f) show simulated S_2 amplitude and phase images at $\omega = 1730 \text{ cm}^{-1}$, where PMMA exhibits a strong near-field phase response corresponding to the absorption caused by the C = O bond stretching [33]. The interior of the PMMA square and the Si substrate show uniform near-field signal as expected, whereas a small dip and spike in S_2 amplitude can be seen near the square edge. These fringe-like patterns parallel to the sample edge can be best seen in the line profiles across the edge as shown in Fig. 2(g) and (h). This is the 'edge darkening' effect usually observed in s-SNOM imaging [34,35], which is documented in the literature and well reproduced by our simulations.

Next, we investigate the edge-darkening effect and the underlying mechanism. To isolate the pure topography-induced near-field signal and eliminate the contrast due to the dielectric function difference in PMMA and Si, we perform simulations on a Si square on top of the Si substrate. The height of the square denoted by s plays an important role in the contrast, as shown in Fig. 3(a). The line profiles are vertically shifted in equal spacing for clarity. Several observations can be made. First, a signal minimum right at the edge of the square is observed. This signal minimum as a function of s is plotted in the left inset in Fig. 3(a). A fast decay and plateau are observed. Secondly, a maximum in the S_2 amplitude exists right after the edge. This maximum value does not exhibit a monotonic behavior as a function of s as shown in the right inset in Fig. 3(a).

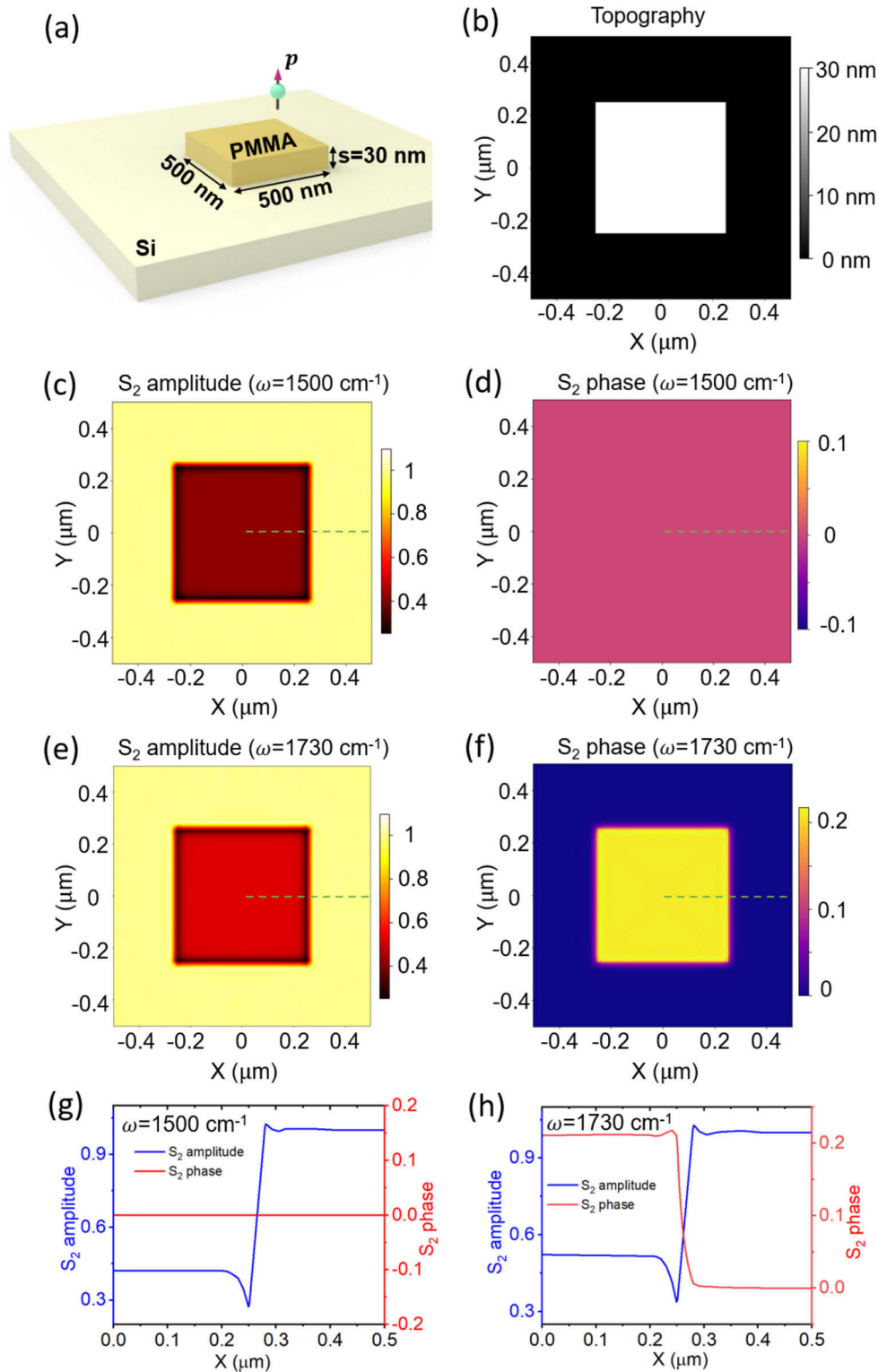


Fig. 2. Near-field contrast on a PMMA square on Si substrate. (a) Schematics of the PMMA square on Si substrate. (b) The topography image corresponding to the tip position as it scans over the PMMA square. (c) and (d) The simulated S_2 amplitude and phase images at $\omega = 1500$ cm^{-1} . (e) and (f) The simulated S_2 amplitude and phase images at 1730 cm^{-1} . The line profiles (green dashed line in (c) to (f)) are shown in (g) and (h) to showcase the edge darkening effect often observed experimentally.

For both small and large s values the maximum is weak, only a few percent higher than the usual Si response. Only when $s \sim 2a$ the maximum is prominent ($\sim 30\%$ higher than the bulk Si response). To understand the edge-induced contrast, we plot the surface charge density for different point-dipole positions X and different step heights s as shown in the table in Fig. 3(b). For this plot the tip is kept at a constant height of $z + a = 80$ nm. Note that the edge is located precisely at $X = 1 \mu\text{m}$. When the point-dipole is located at $X = 0.8 \mu\text{m}$, the charge distribution is identical for different values of s because the edge is too far to have an electromagnetic impact at the point-dipole. Therefore away from the edge ($X < 0.9 \mu\text{m}$ or $X > 1.1 \mu\text{m}$) the near-field signal is identical to that in homogenous bulk Si. When the point-dipole is at $X = 1 \mu\text{m}$, the surface charge density presents a semi-circular distribution on the top surface of the square. For small s , additional surface charge is accumulated on the other side of the edge. This charge contributes to the field at the point-dipole and subsequently to the S_2 signal. As s increases, the charge on the higher side of the step is constant while the charge on the lower side rapidly diminishes, which leads to the decreased S_2 amplitude, explaining the observation in the left inset of Fig. 3(a). On the other hand, when the point-dipole is on the lower side of the step ($X = 1.03 \mu\text{m}$), the point-dipole not only interacts with the bottom surface but also with the wall. When s is small, the charge on the wall is negligible. When s is large the surface charge on the wall is reminiscent of an image dipole with opposite orientation. This dipole-dipole interaction boosts the field at the tip dipole, leading to the observed maximum in S_2 amplitude. In this scenario, one expects the same signal enhancement at larger s . However, as shown in the right inset of Fig. 3(a), this enhanced S_2 gradually disappeared with $s > 60$ nm. This is because for large s , the dipole-dipole interaction with the step wall is not strongly modulated by the tip oscillation. Therefore, demodulation at higher harmonics of the tip oscillation frequency filters out this tip-wall interaction, leading to a minimal signal increase in S_2 . Only when s is comparable to a , the interaction is sensitive to z and contributes to the demodulated signal. Note that in real samples, instead of an ideal vertical edge, the edge typically has a finite slope. This could potentially induce differences in the observation and should be addressed carefully.

We reiterate that one of the important advantages of the PDM is an easy-to-interpret physical picture. However, a quantitative comparison between simulated and experimental data requires caution since the experimental situation is often more complicated. For example, inappropriate AFM scanner feedback settings could lead to bad tip contact while it scans over a sharp edge. As the near-field signal is very sensitive to the tip-sample distance, poor tip contact can easily lead to a significant decrease in near-field signal, which is different from the edge darkening effect discussed above. Furthermore, many commercial AFM tips have a large opening angle (Supplement 1). This often leads to the interaction of the tip shank to the edge [36], resulting in a different contrast mechanism. In addition, as previously noted, the far-field effects such as secondary reflections of the incident and scattered light are not explicitly considered in our current simulation. Such an effect could also lead to anomalous near-field signal contrast especially when a topographically complex surface is present. This could in principle be studied using electrodynamic simulations with far-field incident light under the same framework. Nonetheless, the PDM employed here still offers clear physical insight and qualitative agreement in understanding the long-standing problem of the topography-induced near-field signal contrast.

3.2.2. Surface protrusion and cavity

Another topography feature that one often encounters when performing s-SNOM measurements refers to small surface imperfections such as nanoscale protrusions and cavities. They can be naturally occurring or originate from sample preparation and handling processes. These surface features would inevitably lead to near-field signal contrast that is often confused with the optical properties of the materials. The geometry of these defects can be irregular but as an approximation, we idealize them as hemispheroidal on a flat surface as schematically shown

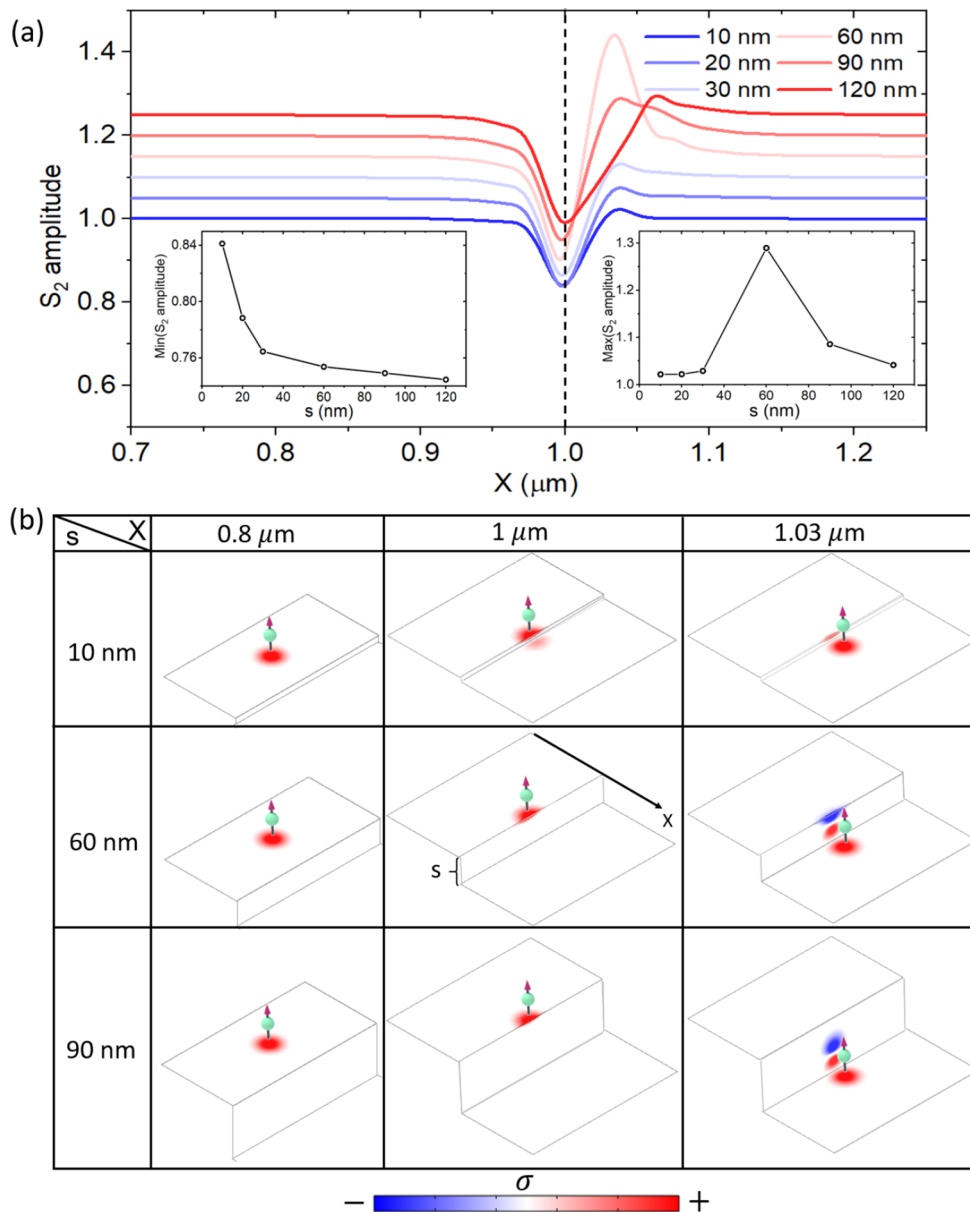


Fig. 3. Near-field contrast across a sharp Si edge. (a) The line profiles of S_2 amplitude across the edge of different heights s on a Si surface. The lines are vertically shifted by equal spacing for a clearer display. The left inset shows the signal at the edge as a function of s (corresponding to the minimal values), where an exponential-like decay is observed. The right inset shows the signal after the edge (corresponding to the maximal values), where a non-monotonic behavior is observed. (b) The surface charge distribution at different point-dipole positions as it scans over the square edge.

in Fig. 4(a). As a concrete example, we fix the in-plane semi-axis length of the spheroid to be $2a = 60$ nm and the out-of-plane semi-axis length as a variable h . In our notation, positive h corresponds to surface protrusion and negative h represents surface cavity.

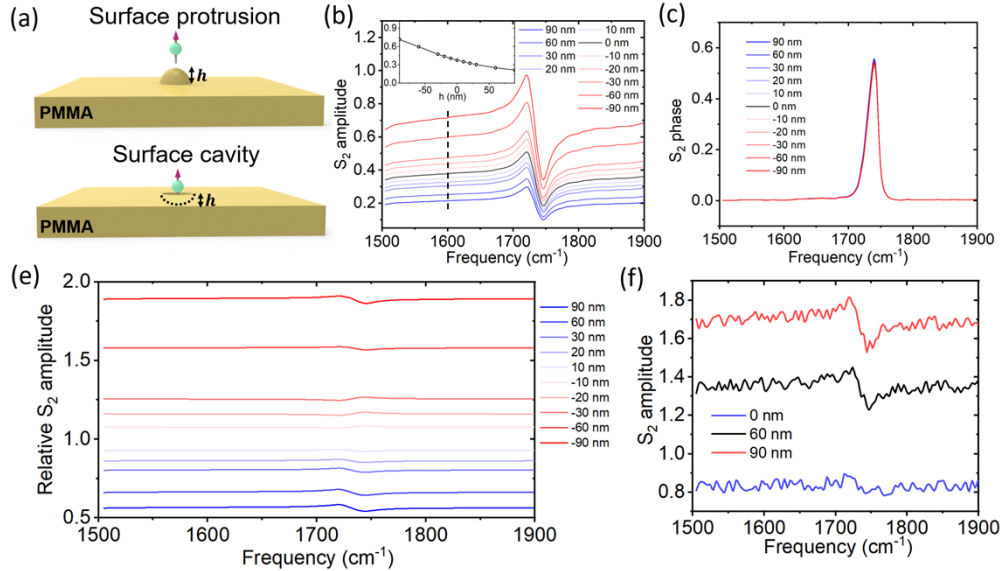


Fig. 4. Surface topography induced near-field signal suppression and enhancement. (a) Schematics of the geometry used to model surface defects. (b) and (c) S_2 amplitude and phase spectra on PMMA for different values of h . The spectra are normalized to S_1 . The inset in (b) displays the S_2 amplitude at 1600 cm^{-1} indicated by the dashed line as a function of h . A nearly linear relationship is observed. (e) The relative S_2 amplitude defined as $S_2(h)/S_2(h=0)$. (f) S_2 amplitude spectra for 3 nm PMMA thin film deposited on a surface cavity with different values of h . The cavity enhances the signal level and the contrast of the PMMA spectra. Random noise is added to each spectrum to mimic real experimental noise with a SNR of 15. Note that the curves in (e) and (f) are not shifted vertically.

First, we simulate the spectroscopic response of PMMA with the point-dipole located at the center of the defect. The amplitude and phase spectra are shown in Fig. 4(b) and (c). Clear spectral contrast is observed predominantly in the amplitude spectra while the phase spectra are nearly inert to this topographic feature. When a surface protrusion is present the spectral signal is generally suppressed while in the case of a surface cavity the signal is elevated. This phenomenon is consistent with experimental observations that have been well known. Yet its mechanism has not been carefully examined. The inset in Fig. 4(b) shows the S_2 amplitude at 1600 cm^{-1} as a function of h . A monotonic and nearly linear relationship is observed. For weak resonator such as PMMA, this topography-induced contrast is insensitive to the material property, as can be seen on the relative S_2 amplitude spectra in Fig. 4(e), where the relative S_2 is defined as $S_2(h, \omega)/S_2(h=0, \omega)$. For strong resonators such as SiO_2 , the situation is much more complicated (Supplement 1).

This finding immediately opens up several interesting perspectives. For example, a desired enhancement of the near-field signal. Similar ideas have been demonstrated by using a resonant substrate, plasmonic antenna, and graphene nano-disk [31,37,38]. To further illustrate this concept, we demonstrate that depositing a thin film on a nanoscale cavity can boost the near-field signal and contrast. 3 nm PMMA film is deposited on top of a Si substrate with a surface cavity. In experimental conditions where the optical alignment is not optimized, the spectral feature of

PMMA can be easily overwhelmed by the noise. Simulated spectroscopy results with random noise added at a signal-to-noise ratio (SNR) of 15 are shown in Fig. 4(f). When the Si substrate is flat ($h = 0$ nm), the weak resonance fingerprint is overwhelmed by the noise. On the other hand, when the thin film is deposited inside the surface cavity, both the absolute signal and the contrast are strongly boosted (by almost 100%), making the spectral fingerprint more easily identifiable. This method is especially suitable for characterizing thin polymers, molecules, and van der Waals crystals as they often exhibit weak vibrational resonances in the IR frequency range and can be easily transferred to arbitrary substrates [33,39–41]. However, additional attention needs to be paid as the strain induced by the protrusion or cavity could potentially alter the intrinsic properties of some materials.

Next, we examine the topography-induced contrast by surface protrusion and cavity in Si and attempt to understand the contrast mechanism. The result is displayed in Fig. 5(a). The trend is similar to that in the inset of Fig. 4(b). The projected surface charge distribution inside the protrusion (top row) and cavity (bottom row) are portrayed in Fig. 5(b) for $|h| = 60$ nm (left column) and $|h| = 90$ nm (right column). This immediately leads to an intuitive physical picture. When the point-dipole is above a surface protrusion, the induced charge is further away from the point-dipole due to the concave curvature. The increased distance causes weaker electric field on the dipole, i.e. G . In the cavity case the convex curvature forces the induced charge closer to the dipole, leading to stronger induced electric field. That is, when the tip is inside a cavity the near-field interaction is enhanced. The larger $|h|$ the more prominent this effect becomes.

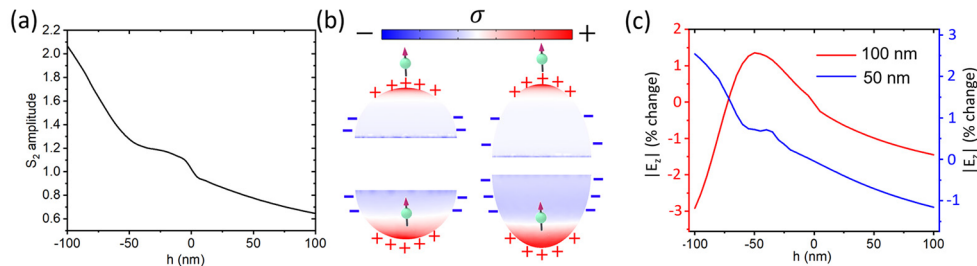


Fig. 5. Comparison of electric field under the tip E_z and the scattering amplitude S_2 . (a) S_2 amplitude as a function of h on Si. (b) The projected charge distributions for 60 nm protrusion (top left), 90 nm protrusion (top right), 60 nm cavity (bottom left), and 90 nm cavity (bottom right). (c) The vertical component of the electric field between the dipole and the sample surface for $z + a = 100$ nm and 50 nm. The y-axis is the percentage change compared to that at $h = 0$ nm.

Instead of the demodulated dipole moment, it is a common practice to use the vertical direction electric field $|E_z|$ between the dipole and the sample to simulate the experimentally measured near-field signal [42–45]. This simplified method does offer a good qualitative simulation in some cases. However, the choice of the simulation parameters is often ad hoc and the relative contrast is not quantitatively reliable [24]. For example, the position where the field is evaluated and the dipole-sample distance have a significant impact on the result. In Fig. 5(c) we plot the electric field intensity in the vertical direction evaluated halfway between the point-dipole and the sample surface for two dipole-sample distances as a function of h . Compared to Fig. 5(a), we see that the change in $|E_z|$ is in the order of 1% as h varies from -100 nm to 100 nm, which is orders of magnitude smaller than the change in S_2 . This is due to the background field created by the dipole being much stronger than the field generated by the induced surface charge. $|E_z|$ is not sensitive to the background field due to the demodulation procedure. For 50 nm tip-sample distance, the $|E_z|$ curve shows a qualitatively similar trend as S_2 while for 100 nm tip-sample distance the trend

between $|E_z|$ and S_2 is totally different. Therefore, when exploring the near-field contrast, our method of calculating S_2 should be preferred against simply plotting $|E_z|$.

3.2.3. Finite size effect

Finally we wrap up our investigation of topographically heterogeneous samples by studying the influence of sample lateral size on the near-field contrast. Although s-SNOM is known to have a ~ 10 nm spatial resolution only limited by the tip apex radius of curvature [23,24], it is important to realize that the information collected by the tip at one location is not solely from a 10 nm by 10 nm area under the tip. This is evident by the experimental observation of the strongly size-dependent near-field contrast even when the size of the feature is orders of magnitude larger than the tip apex [39,46–48]. It should not come as a surprise since the spatial distribution of the tip-enhanced electric field spatially extends over a volume that is larger than the tip apex even though the strongest enhancement occurs within the size of the tip apex. Here we aim to reproduce and study this phenomenon using our point-dipole formalism. First we investigate 30 nm thick PMMA disk with various radius r on Si substrate. The simulated S_2 as a function of r at 1500 cm^{-1} is shown in the bottom left panel of Fig. 6(a), which shows that the near-field signal saturates at around $r = 60$ nm. The top and bottom right panels show the S_2 amplitude and phase spectra on disks with various r . Both the amplitude and phase diminish as decreasing r . As a comparison, we simulate 30 nm thick gold with various radius r on Si substrate as shown in Fig. 6(b). For gold disk the saturation radius seems to be larger than 100 nm, significantly larger than that of the PMMA disk. We attribute this to the near field being much stronger in gold. Consequently, the laterally extended stray field exhibits a more significant impact on gold than PMMA.

Next we simulate the near-field response of a gold particle with varying radius on Si substrate as the results shown in Fig. 6(c). Here, the near-field amplitude does not monotonically increase with particle size since there are two competing effects in action: the lateral and the vertical field extension. For example, from $r = 1\text{ nm}$ to $r = 10\text{ nm}$ the tip is lifted further away from the Si substrate, while the lateral size of the gold particle is not sufficiently increased to compensate the signal loss induced by this increasing tip-substrate distance. The net effect is a dip in the S_2 amplitude. In the case of the disk, only the lateral field extension plays a role and thus a monotonic near-field amplitude is observed. The skin effect does not show to be important in our simulations. However, when the penetration depth of the field is comparable or larger than the material thickness, the contrast could exhibit a different behavior.

Lastly we simulate near-field images on 30 nm thick PMMA disks with 50 nm, 100 nm, and 200 nm radius on Si substrate as shown in Fig. 6(d). Again, the edge darkening effect is observed. More importantly, the size-dependent near-field contrast between 50 nm disk and 100 nm disk can be clearly seen in the line profiles shown in Fig. 6(e) (indicated by the red arrow). Our PDM simulations together with previous experimental observations [39,46–48] demonstrate that the measured near-field signal starts to depend on sample topography information at a critical disk radius $r_c \sim 100$ nm. Any samples below this size starts to exhibit strong size-dependent response. However, for realistic AFM tip this number is expected to be larger as the field around a realistic tip is more comparable to a monopole than a dipole [12]. Clearly the dipole field is more confined than the monopole field. Therefore the PDM likely underestimates the spatial extension of the field as discussed in Supplement 1. This also explains why the PDM often underestimates the penetration depth of the field [32].

3.3. Mapping surface plasmon polaritons in a graphene nanostructure

A tremendously successful research field involving s-SNOM is the spatial mapping of surface plasmon polaritons in van der Waals crystals [4,17,49–51]. In polariton imaging, the tip-launched polariton manifests itself as fringes parallel to the reflecting surface with periodicity $\frac{\lambda_p}{2}$ in

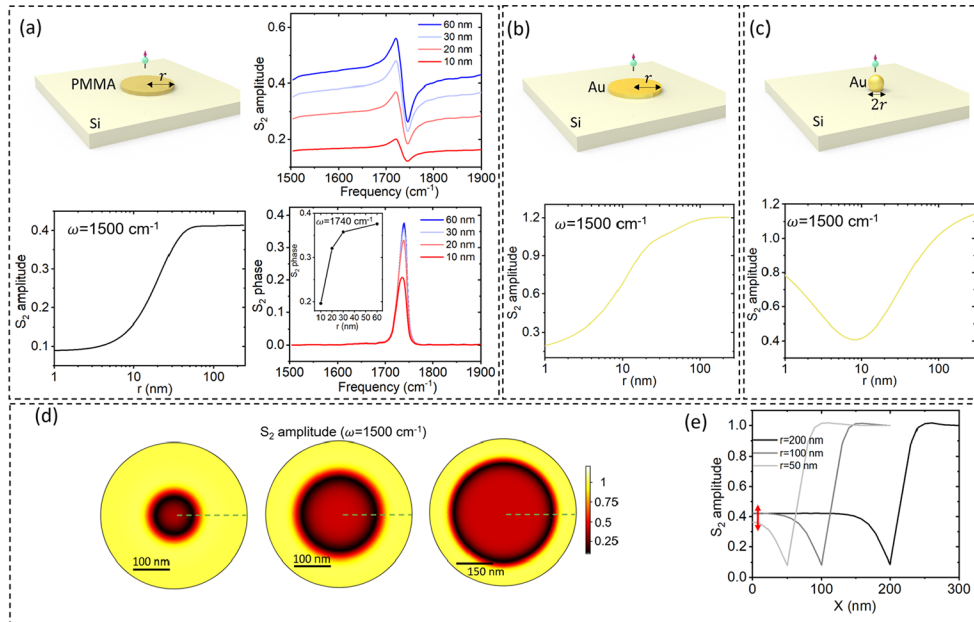


Fig. 6. Simulated size-dependent near-field signal. (a) radius dependent S_2 amplitude and phase spectra (right panel) at the center of a 30 nm thick PMMA disk with radius r on Si substrate. Inset in the bottom right panel shows the S_2 phase at the absorption peak as a function of r . S_2 amplitude at 1500 cm^{-1} is shown in the left bottom panel. For disk radius below 100 nm, a significant decrease in near-field amplitude is observed. (b) radius dependent S_2 amplitude at the center of a 30 nm thick gold disk with radius r on Si substrate. (c) S_2 amplitude at the center of a gold particle with radius r on Si substrate. (b) and (c) are simulated at 1500 cm^{-1} . (d) Simulated S_2 amplitude images of a 30 nm thick PMMA disk with 50 nm (left), 100 nm (center), 200 nm (right) radius on Si substrate. (e) The line profiles taken along the green dashed lines in images in (d). The difference in S_2 amplitude due to the lateral size is indicated by the red arrow. All spectra and images in this figure are normalized to that on Si.

near-field images, where λ_p is the polariton wavelength. However, complications exist so an accurate simulation method is of great interest. For example, upon reflection the polariton in graphene is known to pick up an anomalous phase shift [52]. In addition, when the polariton medium is fabricated as nanostructures whose size is comparable to λ_p , complex interference patterns occur where no clear periodicity can be found [53].

Our generalized PDM also provides a suitable platform for simulating polaritons in structures with arbitrary size and geometry. Next we demonstrate its usefulness by taking as an example the case of a graphene nano-disk, as inspired by the previous studies [31,45]. To model graphene, its 2D optical conductivity is calculated using the random phase approximation [15,49], in which we set the Fermi level to 0.4 eV and the damping rate to 0.33 ps as an example. For numerical reasons, graphene is modeled as a 3D thin layer with thickness $d \ll a$. The 3D conductivity can be calculated as $\sigma_{3D} = \sigma_{2D}/d$. A graphene nano-disk of 300 nm radius on SiO_2 substrate is simulated. To obtain the near-field images, the point dipole is raster scanned, following the same procedure as in the previous sections. The simulated near-field images at three different characteristic frequencies are shown in Fig. 7(a), (b), and (c). A strongly frequency-dependent pattern is observed due to the change of λ_p , corresponding to the different breathing modes resonances. This can be understood by investigating the plasmon dispersion in graphene, which is conveniently visualized as the poles in the imaginary part of the p-polarized frequency- and

momentum-dependent reflection coefficient $Im(r_p(\omega, q))$, as shown in Fig. 7(d). Avoided crossing is observed at around 800 cm^{-1} due to the weak phonon resonance in the SiO_2 substrate.

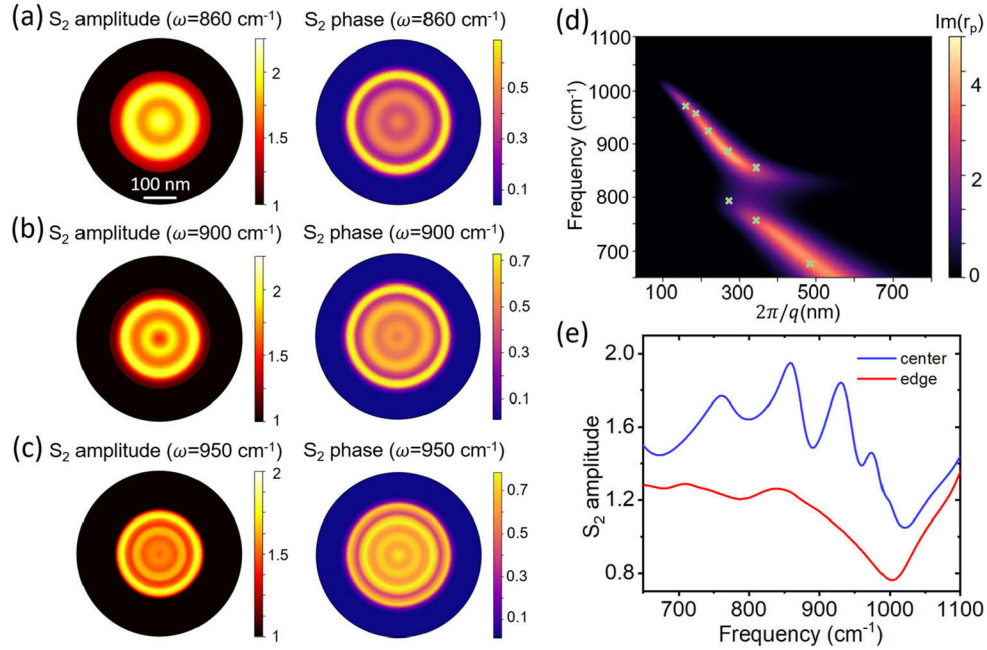


Fig. 7. Simulation of a graphene disk in real and spectral space. (a), (b), and (c), S_2 amplitude (arbitrary unit) and phase images for a graphene nano-disk of 300 nm radius at 860 cm^{-1} , 900 cm^{-1} , and 950 cm^{-1} , respectively. The Fermi level of graphene is 0.4 eV and the damping rate is 0.33 ps. The scale bar (100 nm) in (a) applies to all figures. (d) Plasmon dispersion in graphene on SiO_2 substrate shown as the false colormap of $Im(r_p(\omega, q))$ calculated using the transfer matrix method. (e) S_2 amplitude spectra with the point-dipole at the center of the disk (blue curve) and the edge of the disk (red curve). The plasmon frequency and wavelength extracted from the peaks and valleys in the disk center spectrum is denoted as green crosses in (d).

To associate the near-field images to the dispersion relation, spectroscopy simulations are performed with the point-dipole located at the disk center and the disk edge. The simulated S_2 amplitude spectra are shown in Fig. 7(e). In the disk center, the spectrum exhibits multiple oscillations, corresponding to the breathing modes. The resonance condition is given by $\frac{2r}{\lambda_p} - 0.75 = n$ for $n = 0, 1, 2, \dots$, where 0.75 corresponds to the aforementioned anomalous phase shift due to reflection [31]. Therefore, plasmon wavelength can be easily determined from the spectrum. The extracted plasmon frequency and wavelength are plotted as green crosses in Fig. 7(d), which follow the dispersion curve as expected. The spectrum on the disk edge only shows a weak oscillation. This is due to the circumference of the disk is much larger than λ_p , where strong resonance does not form.

We note here again that in previous studies it was common to simulate the near-field images on surface polariton media such as graphene and MoO_3 using a fixed point-dipole source [44,45]. In such a simulation the near-field signal is represented by the electric field intensity between the dipole and the sample. This type of simulation does not consider the back-action of the sample response to the dipole and thus lacks physical rigor as the tip-sample interaction in most cases should be considered. Although similar spatial polariton interference patterns can often be

observed using both simulation methods, differences in signal contrast can occur (Supplement 1). Further studies with experimental data are required on this topic.

3.4. Strong near-field excitation of the plasmonic optical antenna

In some cases, besides the near-field excitation mediated by the tip, the far-field incident light plays a crucial role as well. A prominent example is the s-SNOM imaging of plasmonic structures such as plasmonic antennas and metamaterials. As demonstrated in numerous studies, s-SNOM imaging can qualitatively map the electric field distribution above the plasmonic antennas [54–58]. In this type of experiments a dielectric tip instead of the typical metal-coated tip is favorable as the near-field created by the dielectric tip is negligible. To a good approximation the antenna is only excited by the far-field incident light. The near-field created by the antenna polarizes the dielectric tip, leading to tip scattering. This way the plasmonic response of the antenna is solely responsible for the detected signal, making s-SNOM imaging a suitable tool for characterizing the intrinsic antenna behavior. A previous study has reported a novel simulation method for this scenario [59]. Conversely, when a metal-coated tip is used, the near-field initiated by the tip also plays an important role, making the detected tip scattering signal a result from the antenna plasmonic field excited by both the far-field incident light and the enhanced near-field under the tip. The precise imaging contrast requires careful consideration of the coupling between the antenna and the tip [59]. This situation is rarely discussed in the literature due to the lack of an efficient modeling platform.

Here we demonstrate that our extended PDM can be employed to reveal the tip-antenna coupling, leading to novel insights in the imaging contrast and augmenting the previously reported simulation method applicable for weakly scattering tips [57,59]. Two limits corresponding to the weak and strong tip scattering are discussed next. When the tip is a weak scatterer, it is considered to be solely polarized by the antenna field. In this case we have

$$\mathbf{p} = \alpha \mathbf{E}_{ant}, \quad (5)$$

where \mathbf{E}_{ant} is the field created by the antenna under incident light excitation. In the strong tip scattering limit, the tip creates very strong near field such that the antenna is only excited by the tip field instead of the far-field incident light. In this limit the role of the plane wave is only to excite the dipole moment of the tip so we have

$$\mathbf{p} = \alpha(\mathbf{E}_{ext} + \mathbf{G}\mathbf{p}). \quad (6)$$

It is important to realize that both the weak and strong tip scattering limits are mathematical idealizations. In reality, both the near-field and far-field excitations are important for the antenna response and tip scattering, especially when a metal-coated tip is used. The general self-consistent vector dipole moment can be written as

$$\mathbf{p} = \alpha(\mathbf{E}_{ext} + \mathbf{G}\mathbf{p} + \mathbf{E}_{ant}), \quad (7)$$

In the above relations the full polarizability tensor is considered due to the fact that x and y components of the field are often comparable to the z component and thus can not be ignored. Since the polarizability along the vertical direction is significantly larger than the other directions, anisotropic polarizability can in principle be considered. For simplicity we consider an isotropic polarizability tensor such that $\alpha_x = \alpha_y = \alpha_z = \alpha$. For rigorosity, the far-field scattering recorded by the detector at a specific direction from \mathbf{p} needs to be carefully calculated [59,60], but here we use the approximation that the total scattered field is the average of that from p_x , p_y , and p_z . As we will show, this approximation already gives a very good qualitative prediction. Note that \mathbf{G} is a tensor whose element G_{ij} ($i, j = x, y, z$) represents the i component of the field at the point-dipole position induced by a unit dipole in the j direction. G_{ij} can be obtained by simulating

the induced field at the dipole position from a unit dipole pointing at x , y , and z direction individually. Equation (7) provides a way to simulate the dipole moment and subsequently the near-field signal beyond the weakly scattering tip limit. The details can be found in [Supplement 1](#).

As a concrete example, a $1\ \mu\text{m}$ long gold antenna on a dielectric substrate ($\epsilon_{\text{sub}} = 4$) is investigated for two polarization situations as depicted in Fig. 8(a). In the simulation, the external illumination is a plane wave. For s-polarized incidence the unit wavevector $\hat{k} = \left(0, \frac{\sqrt{2}}{2}, -\frac{\sqrt{2}}{2}\right)$ and for p-polarized incidence $\hat{k} = \left(\frac{\sqrt{2}}{2}, 0, -\frac{\sqrt{2}}{2}\right)$. This way the antenna can be efficiently excited by the far-field incident light in both cases. Note that in this simulation quasi-electrostatics is no longer valid since the size of the antenna is comparable to the wavelength. The propagation of the dipole field and the retardation effect are of great importance. Therefore, an electrodynamic solver needs to be employed to solve the full set of Maxwell's equations. First we study the weak tip scattering case. The incident field has unit field strength and the self-consistent dipole moment \mathbf{p} is calculated according to Eq. (5). In Fig. 8(b) we show the amplitude of \mathbf{p}/α as a function of X (position across the long axis of the antenna as indicated by the dashed line in Fig. 8(a)) and z (tip-sample distance). For s-polarized incidence, a symmetric response with strong enhancement towards both ends of the antenna is observed, in accordance with the previous report. The hot spots on both ends of the antenna are the signature of its plasmonic dipolar response. For p-polarized incidence, a similar result with a slight asymmetry due to the illumination angle is obtained. On the other hand, in the strong tip scattering limit, the amplitude of \mathbf{p}/α calculated according to Eq. (6) is shown in Fig. 8(c). Clearly it is very distinctive from the weak scattering tip case. The dipole moment is roughly a constant as the tip scans over the antenna.

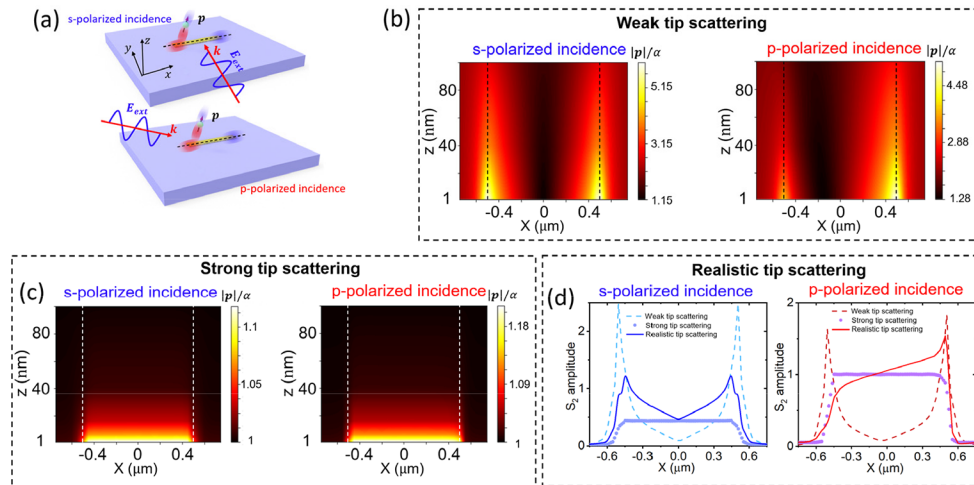


Fig. 8. Simulation of a gold antenna with weak, strong, and realistic tip scattering. (a) Schematics of the simulations of two incidence polarizations. For s-polarized incidence (top) the unit wavevector $\hat{k} = \left(0, \frac{\sqrt{2}}{2}, -\frac{\sqrt{2}}{2}\right)$ and for p-polarized incidence (bottom) $\hat{k} = \left(\frac{\sqrt{2}}{2}, 0, -\frac{\sqrt{2}}{2}\right)$. (b) The simulated amplitude of the self-consistent dipole moment in the weak tip scattering limit as a function of position for s-polarized incidence (left) and p-polarized incidence (right). (c) The simulated amplitude of the self-consistent dipole moment in the strong tip scattering limit as a function of position for s-polarized incidence (left) and p-polarized incidence (right). Vertical dashed lines in (b) and (c) indicate the edge of the antenna. (d) S_2 amplitude (arbitrary unit) for weak tip scattering, strong tip scattering, and realistic tip scattering cases for s-polarized incidence (left) and p-polarized incidence (right).

In an experiment where a metal-coated tip is used, we are in the intermedium of the two limits. That means both the far-field and near-field excitations are crucial ingredients for the measured signal. In this case p should be calculated using Eq. (7). However, it should be noted that the polarizability α is much smaller than that of the antenna due to a^3 being orders of magnitude smaller than the volume of the antenna. That is why the dipole moment for the strongly scattering tip in Fig. 8(c) has a smaller value than that in Fig. 8(b) for the weakly scattering tip. Real AFM tips have a typical shank length $\sim 10 \mu\text{m}$, comparable or even larger than the antenna size in the optical frequency regime. Consequently, to account for the correct relative strength of the far-field and near-field excitations, a phenomenological factor c is added such that the modified Eq. (7) reads

$$p = \alpha(E_{ext} + Gp + cE_{ant}). \quad (8)$$

This c controls the role of the tip. $c = 0$ corresponds to the strong tip scattering limit while $c \rightarrow \infty$ represents the weak tip scattering limit. For realistic tips c takes a finite value and can be used to fit the experimental data. We show in the example below that $c = 0.1$ renders reasonable results. Finally, we demodulate the dipole moment from Eqs. (5), (6), and (8) to obtain the near-field signal as shown in Fig. 8(d) for s-polarized incidence (left) and p-polarized incidence (right). S_2 amplitude for the intermedium case and p-polarized incidence (red solid curve) reproduces the experimental observations very well [61,62].

4. Conclusion and discussions

In summary, we demonstrate a framework that merges the FEM and the PDM to enable simulations of near-field imaging and spectroscopy measurements on arbitrarily heterogeneous sample surfaces. Our highly time-efficient simulation method provides profound physical insights into a wide range of problems involving s-SNOM. More specifically, in a series of proof-of-concept applications we demonstrate its usefulness for the (i) study and understanding of the topography-induced near-field contrast, (ii) surface plasmon polariton in graphene nanostructures, and (iii) plasmonic resonance in plasmonic antennas. Generally, this versatile simulation technique can be applied to analyze any other experimental scenarios that are suitable for PDM approximation. In this article, only isotropic materials are investigated as a proof-of-concept. Material anisotropy can be conveniently incorporated into our general and versatile method. Our proposed method also opens the door for other applications such as generating training data for machine learning [63]. This is of important significance taking into account that training data availability is one of the most severe bottlenecks in the development of artificial intelligence methods, which are currently transforming many fields of science.

It is important to realize that although the PDM has physical merits, the important role of the elongated tip shank should not be overlooked when analyzing the data in a highly quantitative manner. For example, it has been shown that the PDM underestimates the probing depth in s-SNOM and does not capture the strong resonances very well [12,32,47,64]. Although efforts have been devoted to this direction [21–24,31,36,65], efficient methods for simulation of near-field imaging and spectroscopy with realistic tip modeling await more explorations. As demonstrated in a previous study, one method to approximate a spheroidal tip is to place multiple point-dipole inside the spheroid while matching the boundary condition on its surface [49]. This method can be combined with the FEM for arbitrarily heterogeneous sample surfaces. However, a significant increase in simulation time is expected.

Besides s-SNOM, many other tip-enhanced microscopy techniques share the same difficulties with respect to quantitative modeling. Our simulation framework is well suited to serve as a practical starting point and motivate future efforts to simulate other tip-enhanced optical microscopy techniques such as photo-induced force microscopy, peak-force scanning near-field optical microscopy, or tip-enhanced photoluminescence [66–68]. Furthermore, when coupled to other physics processes such as electronic and heat transports, it can be used to model near-field

photocurrent microscopy [69–72] and photothermal microscopy techniques such as AFM-IR [73].

Funding. U.S. Department of Energy (DE-SC0012704); Unitatea Executiva pentru Finantarea Invatamantului Superior, a Cercetarii, Dezvoltarii si Inovarii (OPTIGAN PN-III-P1-1.1-TE-2019-1339); European Cooperation in Science and Technology (COST Action 19118 ESSENCE); Ministerio de Ciencia, Innovación y Universidades (MDM-2016-0618, RTI2018-094830-B-100); Basque Government (IT1164-19).

Acknowledgments. The authors thank Dr. Alexander S. McLeod for the helpful discussion. X.Z.Chen, M.K.Liu, and D.N.Basov acknowledge support from the U.S. Department of Energy, Office of Science, National Quantum Information Science Research Centers, Co-design Center for Quantum Advantage (C2QA) under contract number DE-SC0012704. S.G.Stanciu acknowledges the financial support of UEFISCDI Grant OPTIGAN PN-III-P1-1.1-TE-2019-1339. S.G.Stanciu & M.K.Liu acknowledge the support of COST Action 19118 ESSENCE, which facilitated fruitful interactions. R.H. acknowledges financial support from the Spanish Ministry of Science, Innovation and Universities (national project RTI2018-094830-B-100 and the project MDM-2016-0618 of the Marie de Maeztu Units of Excellence Program) and the Basque Government (grant No. IT1164-19).

Disclosures. The authors declare no conflicts of interest.

Data availability. Data underlying the results presented in this paper are not publicly available at this time but may be obtained from the authors upon reasonable request.

Supplemental document. See [Supplement 1](#) for supporting content.

References

1. F. Keilmann and R. Hillenbrand, “Near-field microscopy by elastic light scattering from a tip,” *Philos. Trans. A. Math. Phys. Eng. Sci.* **362**(1817), 787–805 (2004).
2. R. Hillenbrand and F. Keilmann, “Complex Optical Constants on a Subwavelength Scale,” *Phys. Rev. Lett.* **85**(14), 3029–3032 (2000).
3. M. Liu, A. J. Sternbach, and D. N. Basov, “Nanoscale electrostatics of strongly correlated quantum materials,” *Reports Prog. Phys.* **80**(1), 014501 (2017).
4. W. Ma, P. Alonso-González, S. Li, A. Y. Nikitin, J. Yuan, J. Martín-Sánchez, J. Taboada-Gutiérrez, I. Amenabar, P. Li, S. Vélez, C. Tollan, Z. Dai, Y. Zhang, S. Sriram, K. Kalantar-Zadeh, S.-T. Lee, R. Hillenbrand, and Q. Bao, “In-plane anisotropic and ultra-low-loss polaritons in a natural van der Waals crystal,” *Nature* **562**(7728), 557–562 (2018).
5. X. Chen, X. Fan, L. Li, N. Zhang, Z. Niu, T. Guo, S. Xu, H. Xu, D. Wang, H. Zhang, A. S. McLeod, Z. Luo, Q. Lu, A. J. Millis, D. N. Basov, M. Liu, and C. Zeng, “Moiré engineering of electronic phenomena in correlated oxides,” *Nat. Phys.* **16**(6), 631–635 (2020).
6. A. S. McLeod, J. Zhang, M. Q. Gu, F. Jin, G. Zhang, K. W. Post, X. G. Zhao, A. J. Millis, W. B. Wu, J. M. Rondinelli, R. D. Averitt, and D. N. Basov, “Multi-messenger nanoprobe of hidden magnetism in a strained manganite,” *Nat. Mater.* **19**(4), 397–404 (2020).
7. G. X. Ni, A. S. McLeod, Z. Sun, L. Wang, L. Xiong, K. W. Post, S. S. Sunku, B.-Y. Jiang, J. Hone, C. R. Dean, M. M. Fogler, and D. N. Basov, “Fundamental limits to graphene plasmonics,” *Nature* **557**(7706), 530–533 (2018).
8. M. B. Lundeberg, Y. Gao, R. Asgari, C. Tan, B. Van Duppen, M. Autore, P. Alonso-González, A. Woessner, K. Watanabe, T. Taniguchi, R. Hillenbrand, J. Hone, M. Polini, and F. H. L. Koppens, “Tuning quantum nonlocal effects in graphene plasmonics,” *Science* **357**(6347), 187–191 (2017).
9. P. Schmidt, F. Violla, S. Latini, M. Massicotte, K.-J. Tielrooij, S. Mastel, G. Navickaite, M. Danovich, D. A. Ruiz-Tijerina, C. Yelgel, V. Fal’ko, K. S. Thygesen, R. Hillenbrand, and F. H. L. Koppens, “Nano-imaging of intersubband transitions in van der Waals quantum wells,” *Nat. Nanotechnol.* **13**(11), 1035–1041 (2018).
10. A. S. McLeod, P. Kelly, M. D. Goldflam, Z. Gainsforth, A. J. Westphal, G. Dominguez, M. H. Thiemens, M. M. Fogler, and D. N. Basov, “Model for quantitative tip-enhanced spectroscopy and the extraction of nanoscale-resolved optical constants,” *Phys. Rev. B.* **90**(8), 085136 (2014).
11. B.-Y. Jiang, L. M. Zhang, A. H. Castro Neto, D. N. Basov, and M. M. Fogler, “Generalized spectral method for near-field optical microscopy,” *J. Appl. Phys.* **119**(5), 054305 (2016).
12. A. Cvitkovic, N. Ocelic, and R. Hillenbrand, “Analytical model for quantitative prediction of material contrasts in scattering-type near-field optical microscopy,” *Opt. Express.* **15**(14), 8550 (2007).
13. S. T. Chui, X. Chen, M. Liu, Z. Lin, and J. Zi, “Scattering of electromagnetic waves from a cone with conformal mapping: Application to scanning near-field optical microscope,” *Phys. Rev. B.* **97**(8), 081406 (2018).
14. B. Knoll and F. Keilmann, “Enhanced dielectric contrast in scattering-type scanning near-field optical microscopy,” *Opt. Commun.* **182**(4-6), 321–328 (2000).
15. Z. Fei, G. O. Andreev, W. Bao, L. M. Zhang, A. S. McLeod, C. Wang, M. K. Stewart, Z. Zhao, G. Dominguez, M. Thiemens, M. M. Fogler, M. J. Tauber, A. H. Castro-Neto, C. N. Lau, F. Keilmann, and D. N. Basov, “Infrared nanoscopy of dirac plasmons at the graphene-SiO₂ interface,” *Nano Lett.* **11**(11), 4701–4705 (2011).
16. Q. Lu, A. T. Bollinger, X. He, R. Sundling, I. Bozovic, and A. Gozar, “Surface Josephson plasma waves in a high-temperature superconductor,” *npj Quantum Mater.* **5**(1), 69 (2020).

17. S. Dai, Z. Fei, Q. Ma, A. S. Rodin, M. Wagner, A. S. McLeod, M. K. Liu, W. Gannett, W. Regan, K. Watanabe, T. Taniguchi, M. Thiemens, G. Dominguez, A. H. C. Neto, A. Zettl, F. Keilmann, P. Jarillo-Herrero, M. M. Fogler, and D. N. Basov, "Tunable Phonon Polaritons in Atomically Thin van der Waals Crystals of Boron Nitride," *Science* **343**(6175), 1125–1129 (2014).
18. D. J. Lahneman, T. J. Huffman, P. Xu, S. L. Wang, T. Grogan, and M. M. Qazilbash, "Broadband near-field infrared spectroscopy with a high temperature plasma light source," *Opt. Express* **25**(17), 20421 (2017).
19. M. Eisele, T. L. Cocker, M. A. Huber, M. Plankl, L. Viti, D. Ercolani, L. Sorba, M. S. Vitiello, and R. Huber, "Ultrafast multi-terahertz nano-spectroscopy with sub-cycle temporal resolution," *Nat. Photonics* **8**(11), 841–845 (2014).
20. J. Aizpurua, T. Taubner, F. Javier García de Abajo, M. Brehm, and R. Hillenbrand, "Substrate-enhanced infrared near-field spectroscopy," *Opt. Express* **16**(3), 1529–1545 (2008).
21. P. McArdle, D. J. Lahneman, A. Biswas, F. Keilmann, and M. M. Qazilbash, "Near-field infrared nanospectroscopy of surface phonon-polariton resonances," *Phys. Rev. Res.* **2**(2), 023272 (2020).
22. F. Mooshammer, M. A. Huber, F. Sandner, M. Plankl, M. Zizlsperger, and R. Huber, "Quantifying Nanoscale Electromagnetic Fields in Near-Field Microscopy by Fourier Demodulation Analysis," *ACS Photonics* **7**(2), 344–351 (2020).
23. S. Mastel, A. A. Govyadinov, C. Maissen, A. Chuvilin, A. Berger, and R. Hillenbrand, "Understanding the Image Contrast of Material Boundaries in IR Nanoscopy Reaching 5 nm Spatial Resolution," *ACS Photonics* **5**(8), 3372–3378 (2018).
24. C. Maissen, S. Chen, E. Nikulina, A. Govyadinov, and R. Hillenbrand, "Probes for Ultrasensitive THz Nanoscopy," *ACS Photonics* **6**(5), 1279–1288 (2019).
25. H. Aminpour, L. M. Eng, and S. C. Kehr, "Spatially confined vector fields at material-induced resonances in near-field-coupled systems," *Opt. Express* **28**(22), 32316 (2020).
26. X. Chen, D. Hu, R. Mescall, G. You, D. N. Basov, Q. Dai, and M. Liu, "Modern Scattering-Type Scanning Near-Field Optical Microscopy for Advanced Material Research," *Adv. Mater.* **31**(24), 1804774 (2019).
27. J. Renger, S. Grafström, L. M. Eng, and R. Hillenbrand, "Resonant light scattering by near-field-induced phonon polaritons," *Phys. Rev. B* **71**(7), 075410 (2005).
28. B. M. A. Rahman and A. Agrawal, *Finite Element Modeling Methods for Photonics* (Artech House, 2013).
29. A. Z. Elsherbeni and V. Demir, *The Finite-Difference Time-Domain in Electromagnetics*, Institution of Engineering and Technology, 2015, <http://digital-library.theiet.org/content/books/ew/sbew514e>.
30. W. C. Gibson, *The Method of Moments in Electromagnetics* (Chapman and Hall/CRC, New York, ed. 2nd, 2007).
31. Y. Luan, L. McDermott, F. Hu, and Z. Fei, "Tip- and Plasmon-Enhanced Infrared Nanoscopy for Ultrasensitive Molecular Characterizations," *Phys. Rev. Appl.* **13**(3), 034020 (2020).
32. L. M. Zhang, G. O. Andreev, Z. Fei, A. S. McLeod, G. Dominguez, M. Thiemens, A. H. Castro-Neto, D. N. Basov, and M. M. Fogler, "Near-field spectroscopy of silicon dioxide thin films," *Phys. Rev. B* **85**(7), 075419 (2012).
33. A. A. Govyadinov, I. Amenabar, F. Huth, P. S. Carney, and R. Hillenbrand, "Quantitative Measurement of Local Infrared Absorption and Dielectric Function with Tip-Enhanced Near-Field Microscopy," *J. Phys. Chem. Lett.* **4**(9), 1526–1531 (2013).
34. T. Taubner, R. Hillenbrand, and F. Keilmann, "Performance of visible and mid-infrared scattering-type near-field optical microscopes," *J. Microsc.* **210**(3), 311–314 (2003).
35. C. Liewald, S. Mastel, J. Hesler, A. J. Huber, R. Hillenbrand, and F. Keilmann, "All-electronic terahertz nanoscopy," *Optica* **5**(2), 159 (2018).
36. V. E. Babicheva, S. Gamage, M. I. Stockman, and Y. Abate, "Near-field edge fringes at sharp material boundaries," *Opt. Express* **25**, 23935–23944 (2017).
37. M. Autore, L. Mester, M. Goikoetxea, and R. Hillenbrand, "Substrate Matters: Surface-Polariton Enhanced Infrared Nanospectroscopy of Molecular Vibrations," *Nano Lett.* **19**(11), 8066–8073 (2019).
38. B. T. O'Callahan, M. Hentschel, M. B. Raschke, P. Z. El-Khoury, and S. Lea, *J. Phys. Chem. C*, in press..
39. A. Cvitkovic, N. Ocelic, and R. Hillenbrand, "Material-specific infrared recognition of single sub-10 nm particles by substrate-enhanced scattering-type near-field microscopy," *Nano Lett.* **7**(10), 3177–3181 (2007).
40. F. Huth, A. Govyadinov, S. Amarie, W. Nuansing, F. Keilmann, and R. Hillenbrand, "Nano-FTIR absorption spectroscopy of molecular fingerprints at 20 nm spatial resolution," *Nano Lett.* **12**(8), 3973–3978 (2012).
41. M. Wagner, D. S. Jakob, S. Horne, H. Mittel, S. Osechinskiy, C. Phillips, G. C. Walker, C. Su, and X. G. Xu, "Ultrabroadband Nanospectroscopy with a Laser-Driven Plasma Source," *ACS Photonics* **5**(4), 1467–1475 (2018).
42. F. J. Alfaro-Mozaz, P. Alonso-González, S. Vélez, I. Dolado, M. Autore, S. Mastel, F. Casanova, L. E. Hueso, P. Li, A. Y. Nikitin, and R. Hillenbrand, "Nanoimaging of resonating hyperbolic polaritons in linear boron nitride antennas," *Nat. Commun.* **8**(1), 15624 (2017).
43. J. Duan, R. Chen, Y. Cheng, T. Yang, F. Zhai, Q. Dai, and J. Chen, "Optically Unraveling the Edge Chirality-Dependent Band Structure and Plasmon Damping in Graphene Edges," *Adv. Mater.* **30**(22), 1800367 (2018).
44. G. Álvarez-Pérez, T. G. Folland, I. Errea, J. Taboada-Gutiérrez, J. Duan, J. A. Martín-Sánchez, I. F. Tresguerres-Mata, J. R. Matson, A. Bylinkin, M. He, W. Ma, Q. Bao, J. I. Martín, J. D. Caldwell, A. Y. Nikitin, and P. Alonso-González, "Infrared Permittivity of the Biaxial van der Waals Semiconductor α -MoO₃ from Near- and Far-Field Correlative Studies," *Adv. Mater.* **32**(29), 1908176 (2020).

45. A. Y. Nikitin, P. Alonso-González, S. Vélez, S. Mastel, A. Centeno, A. Pesquera, A. Zurutuza, F. Casanova, L. E. Hueso, F. H. L. L. Koppens, and R. Hillenbrand, "Real-space mapping of tailored sheet and edge plasmons in graphene nanoresonators," *Nat. Photonics* **10**(4), 239–243 (2016).
46. X. Chen, X. Liu, X. Guo, S. Chen, H. Hu, E. Nikulina, X. Ye, Z. Yao, H. A. Bechtel, M. C. Martin, G. L. Carr, Q. Dai, S. Zhuang, Q. Hu, Y. Zhu, R. Hillenbrand, M. Liu, and G. You, "THz Near-Field Imaging of Extreme Subwavelength Metal Structures," *ACS Photonics* **7**(3), 687–694 (2020).
47. W. Zhang and Y. Chen, "Visibility of subsurface nanostructures in scattering-type scanning near-field optical microscopy imaging," *Opt. Express* **28**(5), 6696 (2020).
48. F. Kuschewski, H. G. Von Ribbeck, J. Döring, S. Winnerl, L. M. Eng, and S. C. Kehr, "Narrow-band near-field nanoscopy in the spectral range from 1.3 to 8.5 THz," *Appl. Phys. Lett.* **108**, 113102 (2016).
49. Z. Fei, A. S. Rodin, G. O. Andreev, W. Bao, A. S. McLeod, M. Wagner, L. M. Zhang, Z. Zhao, M. Thiemens, G. Dominguez, M. M. Fogler, A. H. C. Neto, C. N. Lau, F. Keilmann, and D. N. Basov, "Gate-tuning of graphene plasmons revealed by infrared nano-imaging," *Nature* **487**(7405), 82–85 (2012).
50. J. Chen, M. Badioli, P. Alonso-González, S. Thongrattanasiri, F. Huth, J. Osmond, M. Spasenović, A. Centeno, A. Pesquera, P. Godignon, A. Zurutuza Elorza, N. Camara, F. J. G. de Abajo, R. Hillenbrand, and F. H. L. Koppens, "Optical nano-imaging of gate-tunable graphene plasmons," *Nature* **487**(7405), 77–81 (2012).
51. S. S. Sunku, G. X. Ni, B. Y. Jiang, H. Yoo, A. Sternbach, A. S. McLeod, T. Stauber, L. Xiong, T. Taniguchi, K. Watanabe, P. Kim, M. M. Fogler, and D. N. Basov, "Photonic crystals for nano-light in moiré graphene superlattices," *Science* **362**(6419), 1153–1156 (2018).
52. A. Y. Nikitin, T. Low, and L. Martin-Moreno, "Anomalous reflection phase of graphene plasmons and its influence on resonators," *Phys. Rev. B.* **90**(4), 041407 (2014).
53. D. Schrecongost, Y. Xiang, J. Chen, C. Ying, H.-T. Zhang, M. Yang, P. Gajurel, W. Dai, R. Engel-Herbert, and C. Cen, "Rewritable Nanoplasmonics through Room-Temperature Phase Manipulations of Vanadium Dioxide," *Nano Lett.* **20**(10), 7760–7766 (2020).
54. Y. Bao, S. Zu, W. Liu, L. Zhou, X. Zhu, and Z. Fang, "Revealing the spin optics in conic-shaped metasurfaces," *Phys. Rev. B.* **95**(8), 081406 (2017).
55. M. Rahmani, E. Yoxall, B. Hopkins, Y. Sonnefraud, Y. Kivshar, M. Hong, C. Phillips, S. A. Maier, and A. E. Miroshnichenko, "Plasmonic nanoclusters with rotational symmetry: Polarization-invariant far-field response vs changing near-field distribution," *ACS Nano.* **7**(12), 11138–11146 (2013).
56. P. Alonso-González, P. Albella, F. Neubrech, C. Huck, J. Chen, F. Golmar, F. Casanova, L. E. Hueso, A. Pucci, J. Aizpurua, and R. Hillenbrand, "Experimental verification of the spectral shift between near- and far-field peak intensities of plasmonic infrared nanoantennas," *Phys. Rev. Lett.* **110**(20), 203902 (2013).
57. D.-S. Kim and Z. H. Kim, "Role of in-plane polarizability of the tip in scattering near-field microscopy of a plasmonic nanoparticle," *Opt. Express* **20**(8), 8689 (2012).
58. Y. Xu, E. Tucker, G. Boreman, M. B. Raschke, and B. A. Lail, "Optical Nanoantenna Input Impedance," *ACS Photonics* **3**(5), 881–885 (2016).
59. T. Neuman, P. Alonso-González, A. Garcia-Etxarri, M. Schnell, R. Hillenbrand, and J. Aizpurua, "Mapping the near fields of plasmonic nanoantennas by scattering-type scanning near-field optical microscopy," *Laser Photon. Rev.* **9**(6), 637–649 (2015).
60. J. Sun, P. S. Carney, and J. C. Schotland, "Strong tip effects in near-field scanning optical tomography," *J. Appl. Phys.* **102**(10), 103103 (2007).
61. Z. Yao, X. Chen, L. Wehmeier, S. Xu, Y. Shao, Z. Zeng, F. Liu, A. S. McLeod, S. N. Gilbert Corder, M. Tsuneto, W. Shi, Z. Wang, W. Zheng, H. A. Bechtel, G. L. Carr, M. C. Martin, A. Zettl, D. N. Basov, X. Chen, L. M. Eng, S. C. Kehr, and M. Liu, "Probing subwavelength in-plane anisotropy with antenna-assisted infrared nano-spectroscopy," *Nat. Commun.* **12**(1), 2649 (2021).
62. X. Chen, C. F. B. Lo, W. Zheng, H. Hu, Q. Dai, M. Liu, C. Fan, B. Lo, W. Zheng, H. Hu, Q. Dai, and M. Liu, "Rigorous numerical modeling of scattering-type scanning near-field optical microscopy and spectroscopy," *Appl. Phys. Lett.* **111**(22), 223110 (2017).
63. X. Chen, R. Ren, M. Liu, N. Synchrotron, L. Source, and N. York, "Validity of Machine Learning in the Quantitative Analysis of Complex Scanning Near-Field Optical Microscopy Signals Using Simulated Data," *Phys. Rev. Appl.* **10**, 1 (2021).
64. T. Taubner, F. Keilmann, and R. Hillenbrand, "Nanoscale-resolved subsurface imaging by scattering-type near-field optical microscopy," *Opt. Express* **13**(22), 8893 (2005).
65. A. Garcia-Etxarri, I. Romero, F. J. G. de Abajo, R. Hillenbrand, and J. Aizpurua, "Influence of the tip in near-field imaging of nanoparticle plasmonic modes: Weak and strong coupling regimes," *Phys. Rev. B* **79**(12), 125439 (2009).
66. H. Wang, L. Wang, D. S. Jakob, and X. G. Xu, "Tomographic and multimodal scattering-type scanning near-field optical microscopy with peak force tapping mode," *Nat. Commun.* **9**(1), 2005 (2018).
67. M. Almajhadi and H. K. Wickramasinghe, "Contrast and imaging performance in photo induced force microscopy," *Opt. Express* **25**(22), 26923 (2017).
68. B. Yang, G. Chen, A. Ghafoor, Y. Zhang, Y. Zhang, Y. Zhang, Y. Luo, J. Yang, V. Sandoghdar, J. Aizpurua, Z. Dong, and J. G. Hou, "Sub-nanometre resolution in single-molecule photoluminescence imaging," *Nat. Photonics* **14**(11), 693–699 (2020).

69. N. C. H. Hesp, I. Torre, D. Barcons-Ruiz, H. Herzig Sheinfux, K. Watanabe, T. Taniguchi, R. Krishna Kumar, and F. H. L. Koppens, "Nano-imaging photoresponse in a moiré unit cell of minimally twisted bilayer graphene," *Nat. Commun.* **12**(1), 1640 (2021).
70. P. Alonso-González, A. Y. Nikitin, Y. Gao, A. Woessner, M. B. Lundeberg, A. Principi, N. Forcellini, W. Yan, S. Vélez, A. J. Huber, K. Watanabe, T. Taniguchi, F. Casanova, L. E. Hueso, M. Polini, J. Hone, F. H. L. Koppens, and R. Hillenbrand, "Acoustic terahertz graphene plasmons revealed by photocurrent nanoscopy," *Nat. Nanotechnol.* **12**(1), 31–35 (2017).
71. S. S. Sunku, D. Halbertal, R. Engelke, H. Yoo, N. R. Finney, N. Curreli, G. Ni, C. Tan, A. S. McLeod, C. F. B. Lo, C. R. Dean, J. C. Hone, P. Kim, and D. N. Basov, "Dual-Gated Graphene Devices for Near-Field Nano-imaging," *Nano Lett.* **21**(4), 1688–1693 (2021).
72. S. S. Sunku, A. S. McLeod, T. Stauber, H. Yoo, D. Halbertal, G. Ni, A. Sternbach, B.-Y. Jiang, T. Taniguchi, K. Watanabe, P. Kim, M. M. Fogler, and D. N. Basov, "Nano-photocurrent Mapping of Local Electronic Structure in Twisted Bilayer Graphene," *Nano Lett.* **20**(5), 2958–2964 (2020).
73. A. Dazzi and C. B. Prater, "AFM-IR: Technology and Applications in Nanoscale Infrared Spectroscopy and Chemical Imaging," *Chem. Rev.* **117**(7), 5146–5173 (2017).